Nanoscale

PAPER

View Article Online
View Journal | View Issue

Cite this: *Nanoscale*, 2015, **7**, 518

Surface-dominated transport and enhanced thermoelectric figure of merit in topological insulator $Bi_{1.5}Sb_{0.5}Te_{1.7}Se_{1.3}$†

Te-Chih Hsiung,*[a,b,c] Chung-Yu Mou,[d] Ting-Kuo Lee[a,c] and Yang-Yuan Chen*[c,e]

Received 15th September 2014,
Accepted 26th October 2014

DOI: 10.1039/c4nr05376a

www.rsc.org/nanoscale

We report the observation of an order of magnitude enhancement of the thermoelectric figure of merit (ZT = 0.36) in topological insulator $Bi_{1.5}Sb_{0.5}Te_{1.7}Se_{1.3}$ nanowires at 300 K as compared with the bulk specimen (ZT = 0.028). The enhancement was primarily due to an order of magnitude increase in the electrical conductivity of the surface-dominated transport and thermally activated charge carriers in the nanowires. Magnetoresistance analysis revealed the presence of Dirac electrons and determined that the Fermi level was near the conduction band edge. This may be the first thermoelectric measurement of samples with a chemical potential in the gap of a topological insulator without gate tuning, and provides an opportunity to study the contribution of surface states to the Seebeck coefficient and resistivity without concern for the complex effect of band bending.

1 Introduction

The unique electronic structure of gapless surface states and bulk gap[1–5] in topological insulators (TIs) create a unique opportunity for thermoelectric (TE) applications.[6] The efficiency of a TE material is characterized by the dimensionless figure of merit (ZT) (= $S^2T/\rho\kappa$), where T, S, ρ, and κ are the absolute temperature, Seebeck coefficient, electrical resistivity, and thermal conductivity, respectively. Power factor (PF, $S^2\sigma$) enhancement can be achieved by creating a resonant state near the Fermi level because of the drastic change in the electronic density of states.[7] Phonon boundary scattering substantially reduces thermal conductivity in nanowires (NWs),[8,9] and confinement effects are predicted to enhance the PF.[10] After the novel surface state in TIs was discovered, the effect of the nontrivial topology on the TE properties became an appealing research topic.[6,11–13] Because NWs exhibit more surface states than bulk materials or nanoflakes, we were able to observe the novel TE properties of TI NWs. The enhancement of the TE ZT in TIs has been theoretically proposed;[6] however, experimental results have revealed that the TE PF in low-dimensional TIs is still lower than that of their parent bulk materials.[11–13]

Although the TE properties of $Bi_{1.5}Sb_{0.5}Te_{1.7}Se_{1.3}$ (BSTS) bulk materials and nanoflakes have been investigated, NWs of this system have yet to be explored. In this paper, we report the observation of an order of magnitude enhancement of ZT (= 0.36) in TI $Bi_{1.5}Sb_{0.5}Te_{1.7}Se_{1.3}$ NWs at 300 K. The enhancement was primarily due to an order of magnitude increase in the electrical conductivity (2.38×10^5 S m^{-1}) of the surface-dominated transport and thermally activated charge carriers in the NWs, compared with their counterpart BSTS bulk materials. This may be the first TE measurement of samples with a chemical potential in the gap of a TI without gate tuning, and provides an opportunity to study the contribution of surface states to the Seebeck coefficient and resistivity without concern for the complex effect of band bending.

The recently discovered 3D TIs Bi_2Se_3 and Bi_2Te_3 [14–19] are also good TE materials because of their similar characteristics, such as heavy elements and a small band gap. The helical surface state of 3D TIs has been confirmed using surface sensitive techniques, such as angle-resolved photoemission spectroscopy,[14–16] scanning tunneling microscopy,[17–19] and magnetotransport studies.[20–28] The Dirac surface state is protected by time-reversal symmetry, which enables charge carriers to propagate on the surface or along the edge of a TI without backscattering. Because of the high carrier concentration (10^{19} cm^{-3}) of the bulk materials, probing the surface conducting channel is a challenging task. Thus, achieving a high-insulating bulk state is a crucial prerequisite for the transport applications of TI and TE materials.

[a]*Department of Physics, National Taiwan University, Taipei 106, Taiwan. E-mail: techi@phys.sinica.edu.tw*
[b]*Nano Science and Technology Program, Taiwan International Graduate Program, Academia Sinica and National Taiwan University, Taipei, Taiwan*
[c]*Institute of Physics, Academia Sinica, Taipei 11529, Taiwan. E-mail: cheny2@phys.sinica.edu.tw*
[d]*Department of Physics, National Tsing Hua University, Hsinchu 30013, Taiwan*
[e]*Graduate Institute of Applied Physics, National Chengchi University, Taipei 116, Taiwan*

†Electronic supplementary information (ESI) available: Magnetoresistance and thermal conductivity measurements of additional samples. See DOI: 10.1039/c4nr05376a

Recently, the BSTS system was confirmed to be a high-insulating bulk TI with high bulk resistivity[21–23] because of the ordered occupation of Te/Se in the quintuple-layer unit, which substantially cancels the bulk carriers.[21,23] In addition, the low-dimensional nanostructure with a high surface-to-volume ratio allows the metallic surface conduction and TE transport properties to be efficiently probed. In this study, we selected BSTS NWs as our target specimens and expected to observe novel transport and TE properties therein.

2 Experimental method

2.1 Nanowire growth

NWs and nanoribbons were synthesized using a stress-induced method,[29–31] a catalyst-free growth mechanism based on the mismatch of thermal expansion coefficients between the target film and substrate during a thermal annealing process. The thermally induced stress stimulated mass flow along the grain boundaries to form NWs or nanoribbons. The BSTS thin film was deposited using the pulsed laser deposition (PLD) method with 140 mJ at a frequency of 10 Hz. The BSTS bulk for the PLD target was grown using the Bridgman method with mixed Bi, Sb, Te, and Se powder 5 N (99.999%) at a molar ratio of 1.5 : 0.5 : 1.7 : 1.3 in sealed evacuated quartz tubes. The sample was heated to 800 °C for 48 h, followed by cooling slowly to 500 °C and then annealing at that temperature for 96 h.

Fig. 1a shows a scanning electron microscopy (SEM) image of the as-grown NWs several tens of micrometers in length and with diameters ranging from 50 to 300 nm. Straight and uniform BSTS NWs with a high aspect ratio were formed. The high-resolution transmission electron microscopy (TEM) image and the selected area electron diffraction (SAED) pattern revealed that the BSTS NWs were high-quality single-crystalline in a rhombohedral structure with the space group D^5_{3d} ($R\bar{3}m$), growing along the [110] direction (Fig. 1b). The electron dispersion spectroscopy (EDS) line scan profile (Fig. 1c) and elemental mapping images of the BSTS NW (Fig. 1d) indicated that the Bi, Sb, Te, and Se were uniformly distributed throughout the NW. Furthermore, the EDS point scanning of the NWs revealed that the atomic ratio of Bi/Sb/Te/Se was 1.5(±0.3) : 0.36 (±0.2) : 1.63(±0.3) : 1.01(±0.02), which is approximately close to the nominal values of 1.5, 0.5, 1.7, and 1.3, respectively. Fig. 2a shows an SEM image of the device for the Seebeck coefficient and resistivity measurements of a single NW. A line heater was placed on the right hand side of the NW to create a temperature difference across it; the temperatures at the two ends of the NW were monitored using two thermometers by the side. The resistance was measured by the four probe method. Fig. 2b shows a high-magnification SEM image of thermometer 1.

2.2 Device fabrication

The NW specimens were mechanically transferred to the SiO_2 (300 nm)/Si substrate with predefined marks. The electrical contacts were defined using electron-beam lithography and thermal evaporation of Ti/Au.

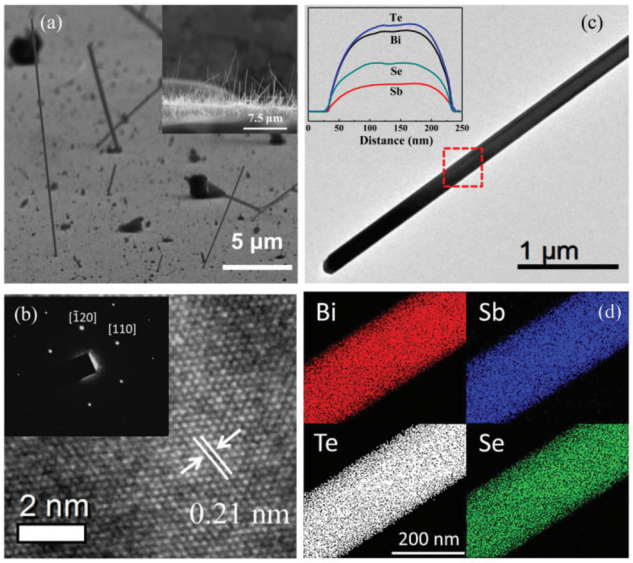

Fig. 1 (a) SEM image of the as-grown NWs. The inset shows a side view of the as-grown NWs. (b) High-resolution TEM image of the BSTS NW showing a clear crystalline structure. The SAED pattern (top left) shows sharp diffraction spots, indicating that the high-quality single-crystal BSTS NW grew in the [110] direction. (c) Scanning TEM image of a BSTS NW. The line profiles show that the Bi, Sb, Se, and Te are homogeneously distributed throughout the NW. (d) The elemental mapping obtained from the EDS scan reveals that Bi, Sb, Se, and Te are uniformly distributed in the BSTS NW.

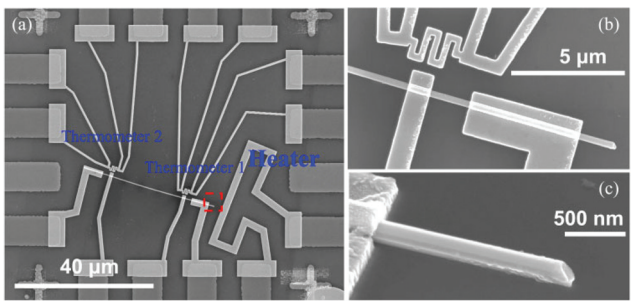

Fig. 2 (a) SEM image of the device for Seebeck coefficient and electrical conductivity measurements. (b) High-magnification SEM image of thermometer 1. (c) Cross-section SEM image of the dashed line area of (a).

2.3 Thermoelectric measurements

Magnetotransport measurements were conducted using a quantum design physical property measurement system. The Seebeck coefficients of the bulk material and NWs were measured using a conventional steady-state method in an Oxford cryostat. The bulk TE properties were also measured using commercial equipment (ZEM-3, ULVAC-RIKO, Japan). The thermal conductivity κ of the BSTS bulk material was calculated using the formula $\kappa = D \times C_p \times d$, where D is the thermal diffusivity, C_p is the specific heat, and d is the density

of the sample. The term D was measured using a laser flash apparatus (NETZSCH, LFA 457). The NW thermal conductivity was measured using the 3ω method (see the ESI† for details).[32,33]

3 Results and discussion

3.1 Temperature dependence of resistance

According to the SEM image of the NW, the cross-section is approximately circular for NW1 with diameter d = 180 nm (Fig. 2c) and ribbon-like for NW2 with width w = 110 nm and thickness t = 375 nm (see the ESI†), which is approximately equivalent to a diameter d = 230 nm nanowire having the same cross-sectional area. The temperature dependence of resistivity for the BSTS NWs is shown in Fig. 3a. The transport behavior of NW1 and NW2 revealed semiconductor-like behavior at less than 300 K, indicating insulating behavior, but this became saturated and further decreased as the temperature decreased to less than 50 K, revealing an additional conduction channel (inset of Fig. 3a).[27] From the fitting of resistance to a 3D variable-range hopping model (3D VRH), R is approximately $\sim e^{(T/T_0)^{-1/4}}$, and a significant deviation occurred at less than 150 K and 120 K for NW1 and NW2, respectively, indicating the existence of a parallel metallic conduction of surface states (inset in Fig. 3b).[23] In addition, the total sheet conductance $G\square$ of a TI with thickness t can be formulated as $G\square = G_s + \sigma_b t$, where G_s is the surface sheet conductance and σ_b is the bulk conductivity. For quantitative calculation the equivalent thickness values $t \sim 180$ nm for NW1 and t = 375 nm for NW2 were used.

At 2 K, $G_s = 2.5 \times 10^{-4}\ \Omega^{-1}$, $\sigma_b = 7.52\ \Omega^{-1}\ cm^{-1}$, surface-dominated transport (approximately 94%) occurred in BSTS NW1, in which the resistivity decreased by a factor of 80 compared with the bulk. At 300 K, the G_s and σ_b values of NW1 and the bulk specimen were $G_s = 24.9 \times 10^{-4}\ \Omega^{-1}$, $\sigma_b = 114.03\ \Omega^{-1}\ cm^{-1}$ and $G_s = 10.95 \times 10^{-4}\ \Omega^{-1}$, $\sigma_b = 25.49\ \Omega^{-1}\ cm^{-1}$, respectively. The resistivity of NW1 was 10 times lower than the bulk (Fig. 3a)[22–24] because of a near 50% surface contribution and the bulk conduction contributed by thermally excited carriers. Remarkably, the stress-induced NW growth method improved the TI surface properties and the crystal quality (less disorder); thus, the thermally activated charge carriers provided bulk conduction at room temperature.

3.2 Thermoelectric properties

Heavy elements produce strong spin orbital coupling in TIs and produce low phonon thermal conductivity in TE materials. In addition, a small band gap in a TE material typically produces a large TE PF, providing an opportunity to modify the band structure of a TI; thus, an intrinsic TI material might be a satisfactory TE material and *vice versa*. The magnitude and temperature dependence of the Seebeck coefficient of the NWs were similar to the BSTS bulk material, monotonically increasing as the temperature increased from 40 to 300 K and achiev-

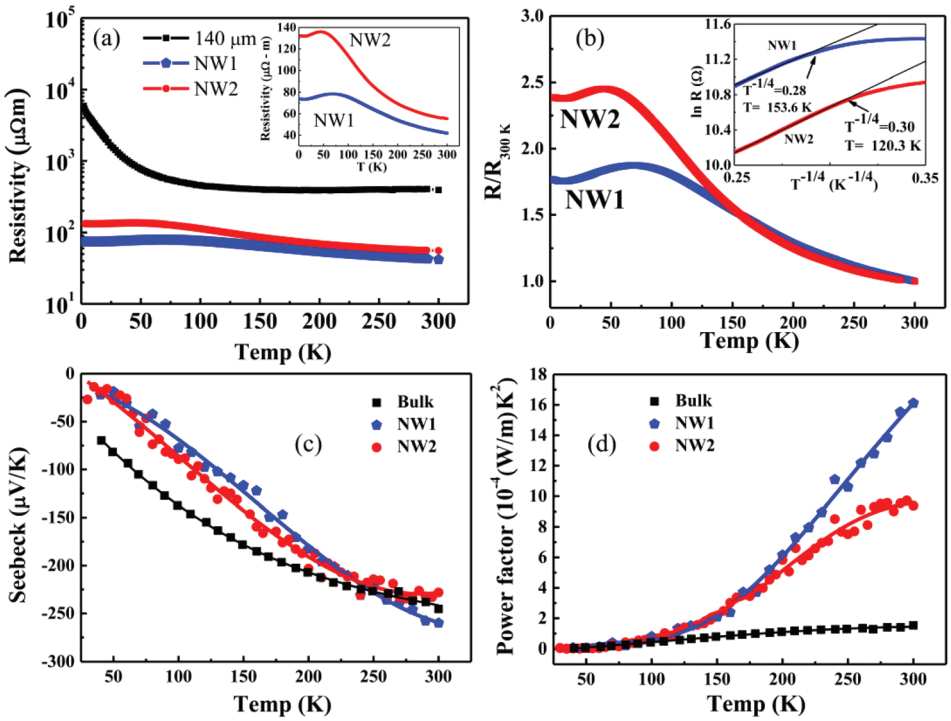

Fig. 3 (a) The temperature dependence of the logarithmic resistivity for BSTS specimens NW1 (180 nm in diameter), NW2 (230 nm in diameter), and the bulk material (thickness of 140 μm). The inset is the resistivity in a linear scale plot for NW1 and NW2. (b) Temperature dependence of the normalized resistance. The inset shows the fitting of the 3D variable-range hopping model. (c) Temperature dependence of the Seebeck coefficient. (d) Temperature dependence of the TE PF.

Table 1 Summary of TE parameters for BSTS NWs and the bulk material, measured at 300 K

BSTS	Diameter (nm)	S (μV K^{-1})	ρ ($\mu\Omega$ m)	PF (10^{-4} W m^{-1} K^{-2})	κ (W m^{-1} K^{-1})	ZT
NW 1	180	−259	41.9	16.11	1.33[a]	0.36
NW 2	230	−228	55.4	9.38	1.33[a]	0.21
Bulk		−235.8	399.5	1.33	1.4	0.028

[a] The value is the average of κ = 1.4 and 1.25 W m^{-1} K^{-1} for NW4 and NW5, respectively (see the ESI).

ing the bulk value at room temperature (Fig. 3c). The Seebeck coefficient of a TI can be formulated using the Boltzmann transport equation:[6]

$$\sigma = e^2 \int_{-\infty}^{\infty} d\varepsilon \left(\frac{\partial f(\varepsilon)}{\partial \varepsilon}\right) \sum(\varepsilon)$$

$$T\sigma S = e \int_{-\infty}^{\infty} d\varepsilon \left(\frac{\partial f(\varepsilon)}{\partial \varepsilon}\right) \sum(\varepsilon)(\varepsilon - E_f)$$

where σ is the electrical conductivity and S is the Seebeck coefficient. The term $\sum(\varepsilon) = N(\varepsilon)\tau(\varepsilon)\nu_x(\varepsilon)^2$ is the conductivity density, and $f(\varepsilon)$ is the Fermi–Dirac distribution function. The ambipolar field effect in TIs has been comprehensively studied; it yields a sign change in the Hall coefficient and a resistance maximum as the Fermi level crosses the charge neutral point of the symmetry protected surface state. In addition to the Hall coefficient, the Seebeck coefficient changing sign as the Fermi level crosses the Dirac point has recently been demonstrated in a Bi_2Se_3 nanoflake.[11] In addition, the theoretical flat-band model[13] indicated that the Seebeck coefficient achieved a maximal value around the band edges. The high Seebeck coefficient observed in this study indicated that the Fermi levels of the two NWs were near the conduction band minimum, which is consistent with the Shubnikov–de Haas (SdH) oscillation analysis discussed later. Consequently, a TE PF enhancement of a factor of 10 in quasi-1D geometry at room temperature was achieved (Fig. 3d). Table 1 shows the comparison of TE parameters for the NWs and the BSTS bulk material.

3.3 Magnetotransport properties

To understand the nature of the surface properties comprehensively, we performed magnetotransport measurements on the NW1 and NW2 specimens. As shown in Fig. 4a, a weak anti-localization (WAL) effect was obtained in the lower field region; the sharp cusps of magnetoresistance (MR) at low temperatures are a signature of the nontrivial Dirac surface state. The WAL in a TI is a quantum correction of classical conductance. The spin-momentum locking mechanism in a TI results from strong spin orbital coupling, in which the surface charge carriers acquire a π Berry phase and propagate along the edge or on the surface without backscattering, because of the destructive interference of time reversed paths.

The high surface-to-volume ratio in the low-dimensional NWs, in which the bulk carriers were suppressed and produced pronounced SdH oscillations, was revealed in the MR. Fig. 4b shows the temperature dependence of resistance for NW1 after a smooth background subtraction. The SdH oscillations of NW1 and NW2 show a period of $(\Delta 1/B)$ = 0.0117 T^{-1}

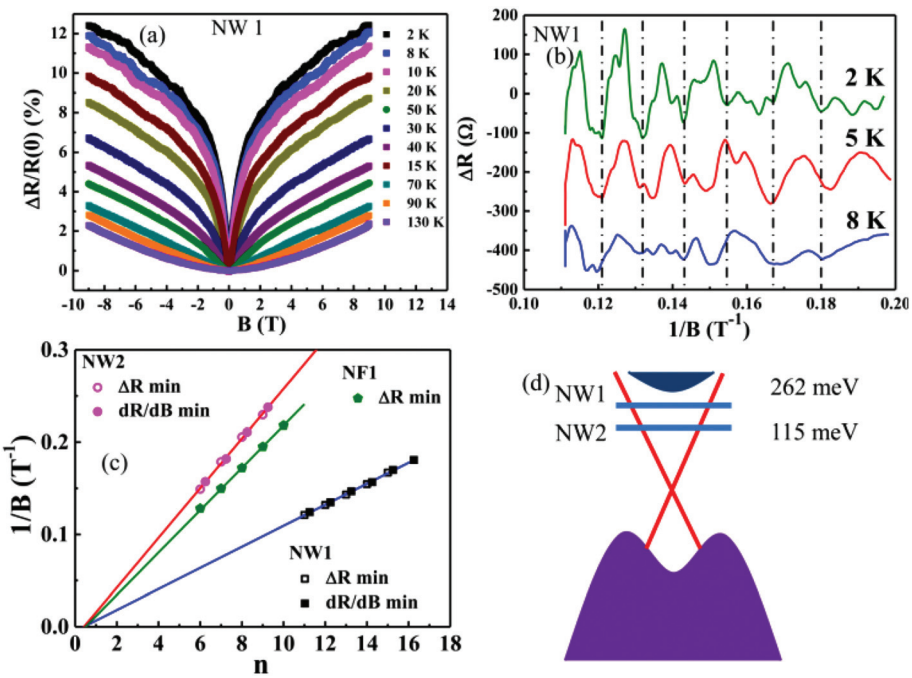

Fig. 4 (a) Transverse magnetoresistance of NW1 at various temperatures. (b) ΔR as a function of $1/B$. (c) Landau level fan diagram plot. NF1 represents the BSTS nanoflake.[21] (d) Schematic of the Fermi level positions for NW1 and NW2.

and $(\Delta 1/B) = 0.02683\ T^{-1}$, respectively, yielding corresponding Fermi surface cross-section areas of $A_F = 8.1 \times 10^{17}\ m^{-2}$ and $A_F = 3.55 \times 10^{17}\ m^{-2}$ according to the Onsager relation. This corresponds to a Fermi wave number of $k_F = 0.0507\ Å^{-1}$ and $0.0336\ Å^{-1}$ and a surface carrier density n_{2D} of $2.05 \times 10^{12}\ cm^{-2}$ and $0.89 \times 10^{12}\ cm^{-2}$ for NW1 and NW2, respectively. Fig. 4c shows the Landau level fan diagram plot of $1/B$ *versus* n for the two NWs. The π Berry phase of the nontrivial topological surface yields the physical origin of the SdH oscillations within the intercept of 0.5 on the n axis. The linear fit of the data yields intercepts of $n = 0.42 \pm 0.12$ for NW1 and 0.43 ± 0.12 for NW2, which are close to the 0.5 value for ideal Dirac fermions. Lifshitz–Kosevich (LK) theory was applied to the SdH amplitudes for NW1 and NW2 with mass $m_c = 0.075\ m_e$[21] to analyze the parameters of TI surface states. The Dingle analysis revealed a scattering time of $\tau = 6.9 \times 10^{-14}$ s, which yielded a surface mobility of $\mu_s = 1616.4\ cm^2\ V^{-1}\ s^{-1}$ and a mean free path of $\ell = 54$ nm for NW1. For NW2, $\tau = 8 \times 10^{-14}$ s, $\mu_s = 1875\ cm^2\ V^{-1}\ s^{-1}$, and $\ell = 41$ nm. The mean free path obtained in this study is similar to that reported in a previous study.[22] Together with m_c and the obtained value of k_F for the NWs, Fermi levels 262 meV and 115 meV higher than the Dirac point (Fig. 4d) and Fermi velocities $v_F = 7.84 \times 10^5\ m\ s^{-1}$ and $v_F = 5.19 \times 10^5\ m\ s^{-1}$ were obtained for NW1 and NW2, respectively. Thus, the high Fermi level positions of the NWs are consistent with the high Seebeck coefficient discussed previously.

For TIs, the linear part of the MR (LMR) usually observed in a high magnetic field has been claimed to be a result of the surface state.[28,34–37] Fig. 4a indicates that the MR becomes more linear as the temperature decreases, which can be described using a quadratic equation $MR = a|H| + b/2H^2$ (in the temperature range of 50 to 130 K). Recently, the LMR was determined to be controlled by mobility and is independent of carrier density, which is complementary to the Hall effect.[38] The LMR can help determine the mobility and carrier density of NWs.[28] As shown in Fig. 5a, we plotted the conventional mobility (μ_{MR}) by the extraction of MR mobility[39,40] and the linear mobility (μ_{LMR}), fitted from the slope dMR/dH, as a function of temperature. The two sets of data coincided perfectly with each other, indicating identical power law dependence. The increase in the mobility of the two NWs as the temperature decreased indicated that phonon scattering dominated in the high temperature region instead of defect scattering. We further plotted the carrier density, as shown in Fig. 5b, according to the obtained value of the mobility. Both the trend and magnitude observed in the temperature dependence of the carrier density and mobility agreed favorably with those of the nanoflake (see the ESI†). The lower carrier concentration further supported the high PF obtained in this study.

The TE transport properties of TIs are the combination of surface and bulk components. We quantitatively analyzed the data of the NWs from a bulk viewpoint. The mobility of the NWs was similar to that of the bulk material ($100\ cm^2\ V^{-1}\ s^{-1}$) at 300 K; however, the carrier density of the NWs ($14 \times 10^{18}\ cm^{-3}$) was 10 times higher without degrading the Seebeck coefficient or mobility, which should be degraded by increasing carrier density according to the Mott relation,[7]

$$S = \frac{\pi^2}{3}\frac{k_B}{q}k_B T\left\{\frac{d[\ln(\sigma(E))]}{dE}\right\}_{E=E_F} = \frac{\pi^2}{3}\frac{k_B}{q}k_B T\left\{\frac{1}{n}\frac{dn(E)}{dE} + \frac{1}{\mu}\frac{d\mu(E)}{dE}\right\}_{E=E_F}.$$

This result is attributed to the high density of states and its derivative as the Fermi level nears the bulk conduction band edge.

4 Conclusions

In summary, we synthesized high-quality single-crystalline TI BSTS NWs by using a stress-induced method. There is no need to have thin films to open the gap as previously proposed.[6] The presence of topological surface states was clearly indicated by magnetotransport measurements. An enhanced thermoelectric figure of merit was observed in the high crystal quality NWs, due to the surface-dominated transport and high-insulating bulk state in the nanowires. From the MR analysis, the high mobility and low carrier density obtained in the two NWs produced a consistently large TE PF. At room temperature, the two NWs exhibited an intrinsic bulk Seebeck coefficient; specifically, the gapless surface states and high Fermi level positions near the bottom of the conduction band were its physical origins.

Additional studies investigating the thermal conductivity with distinct cross-sectional areas are required. The thermal conductivity has been shown to be substantially reduced in NWs.[8,9] Thus, together with the reduction of κ in NWs and the PF enhancement observed in this study, the novel properties of TIs provide a promising direction to enhance the TE ZT further. The high-insulating bulk state in BSTS provides a foundation for TE property studies and facilitates the development of low-power-consumption spintronic devices and quantum computing applications.

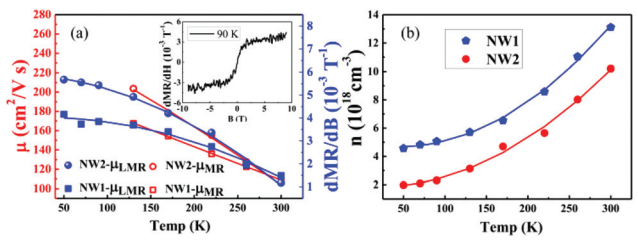

Fig. 5 (a) Extraction of MR mobility and linear part (LMR) of the MR of the NWs. (b) Temperature dependence of the carrier concentration.

Acknowledgements

We thank Rajeshkumar Mohanraman, Hung-Shen Chang, and Li Zhao for their valuable contributions. This work was supported by the National Science Council, Taiwan (grant number NSC 100-2112-M-001-019-MY3). Technical support was provided by the instrument center and the Core Facilities for Nanoscience and Nanotechnology at Academia Sinica, Taiwan.

Notes and references

1 J. E. Moore, *Nature*, 2010, **464**, 194.
2 M. Z. Hasan and C. L. Kane, *Rev. Mod. Phys.*, 2010, **82**, 3045.
3 X. L. Qi and S. C. Zhang, *Phys. Today*, 2010, **63**(1), 33.
4 L. Fu and C. L. Kane, *Phys. Rev. Lett.*, 2008, **100**, 096407.
5 T. D. Stanescu, J. D. Sau, R. M. Lutchyn and S. D. Sarma, *Phys. Rev. B: Condens. Matter Mater. Phys.*, 2010, **81**, 241310(R).
6 P. Ghaemi, R. S. K. Mong and J. E. Moore, *Phys. Rev. Lett.*, 2010, **105**, 166603.
7 J. P. Heremans, V. Jovovic, E. S. Toberer, A. Saramat, K. Kurosaki, A. Charoenphakdee, S. Yamanaka and G. J. Snyder, *Science*, 2008, **321**, 554.
8 A. I. Hochbaum, R. K. Chen, R. D. Delgado, W. J. Liang, E. C. Garnett, M. Najarian, A. Majumdar and P. D. Yang, *Nature*, 2008, **451**, 163.
9 J. W. Roh, S. Y. Jang, J. Kang, S. Lee, J. S. Noh, W. Kim, J. Park and W. Lee, *Appl. Phys. Lett.*, 2010, **96**, 103101.
10 L. D. Hicks and M. S. Dresselhaus, *Phys. Rev. B: Condens. Matter*, 1993, **47**, 16631.
11 D. Kim, P. Syers, N. P. Butch, J. Paglione and M. S. Fuhrer, *Nano Lett.*, 2014, **14**, 1701.
12 B. Hamdou, J. Kimling, A. Dorn, E. Pippel, R. Rostek, P. Woias and K. Nielsch, *Adv. Mater.*, 2013, **25**, 239.
13 M. T. Pettes, J. Maassen, I. Jo, M. S. Lundstrom and L. Shi, *Nano Lett.*, 2013, **13**, 5316.
14 Y. Xia, D. Qian, D. Hsieh, L. Wray, A. Pal, H. Lin, A. Bansil, D. Grauer, Y. S. Hor, R. J. Cava and M. Z. Hasan, *Nat. Phys.*, 2009, **5**, 398.
15 Y. L. Chen, J. G. Analytis, J.-H. Chu, Z. K. Liu, S.-K. Mo, X. L. Qi, H. J. Zhang, D. H. Lu, X. Dai, Z. Fang, S. C. Zhang, I. R. Fisher, Z. Hussain and Z.-X. Shen, *Science*, 2009, **325**, 178.
16 D. Hsieh, Y. Xia, D. Qian, L. Wray, F. Meier, J. H. Dil, J. Osterwalder, L. Patthey, A. V. Fedorov, H. Lin, A. Bansil, D. Grauer, Y. S. Hor, R. J. Cava and M. Z. Hasan, *Phys. Rev. Lett.*, 2009, **103**, 146401.
17 Z. Alpichshev, J. G. Analytis, J. H. Chu, I. R. Fisher, Y. L. Chen, Z. X. Shen, A. Fang and A. Kapitulnik, *Phys. Rev. Lett.*, 2010, **104**, 016401.
18 T. Zhang, P. Cheng, X. Chen, J.-F. Jia, X. Ma, K. He, L. Wang, H. Zhang, X. Dai, Z. Fang, X. Xie and Q.-K. Xue, *Phys. Rev. Lett.*, 2009, **103**, 266803.
19 Y. Zhang, K. He, C. Z. Chang, C. L. Song, L. L. Wang, X. Chen, J. F. Jia, Z. Fang, X. Dai, W. Y. Shan, S. Q. Shen, Q. Niu, X. L. Qi, S. C. Zhang, X. C. Ma and Q. K. Xue, *Nat. Phys.*, 2010, **6**, 584.
20 A. A. Taskin, S. Sasaki, K. Segawa and Y. Ando, *Phys. Rev. Lett.*, 2012, **109**, 066803.
21 T. C. Hsiung, D. Y. Chen, L. Zhao, Y. H. Lin, C. Y. Mou, T. K. Lee, M. K. Wu and Y. Y. Chen, *Appl. Phys. Lett.*, 2013, **103**, 163111.
22 A. A. Taskin, Z. Ren, S. Sasaki, K. Segawa and Y. Ando, *Phys. Rev. Lett.*, 2011, **107**, 016801.
23 Z. Ren, A. A. Taskin, S. Sasaki, K. Segawa and Y. Ando, *Phys. Rev. B: Condens. Matter Mater. Phys.*, 2011, **84**, 165311.
24 B. Xia, P. Ren, A. Sulaev, P. Liu, S.-Q. Shen and L. Wang, *Phys. Rev. B: Condens. Matter Mater. Phys.*, 2013, **87**, 085442.
25 C. H. Lee, R. He, Z. H. Wang, R. L. J. Qiu, A. Kumar, C. Delaney, B. Beck, T. E. Kidd, C. C. Chancey, R. M. Sankaran and X. P. A. Gao, *Nanoscale*, 2013, **5**, 4337.
26 S.-K. Jerng, K. Joob, Y. Kim, S.-M. Yoon, J. H. Lee, M. Kim, J. S. Kim, E. Yoon, S.-H. Chun and Y. S. Kim, *Nanoscale*, 2013, **5**, 10618.
27 Z. Wang, R. L. J. Qiu, C. H. Lee, Z. Zhang and X. P. A. Gao, *ACS Nano*, 2013, **7**, 2126.
28 H. Tang, D. Liang, R. L. J. Qiu and X. P. A. Gao, *ACS Nano*, 2011, **5**, 7510.
29 W. Shim, J. Ham, K. Lee, W. Jeung, M. Johnson and W. Lee, *Nano Lett.*, 2009, **9**, 18.
30 J. Ham, W. Shim, D. H. Kim, S. Lee, J. Roh, S. W. Sohn, K. H. Oh, P. W. Voorhees and W. Lee, *Nano Lett.*, 2009, **9**, 2867.
31 Dedi, P. C. Lee, C. H. Chien, G. P. Dong, W. C. Huang, C. L. Chen, C. M. Tseng, S. R. Harutyunyan, C. H. Lee and Y. Y. Chen, *Appl. Phys. Lett.*, 2013, **103**, 023115.
32 L. Lu, W. Yi and D. L. Zhang, *Rev. Sci. Instrum.*, 2001, **72**, 2996.
33 G. Li, D. Liang, R. L. J. Qiu and X. P. A. Gao, *Appl. Phys. Lett.*, 2013, **102**, 043104.
34 X. Wang, Y. Du, S. Dou and C. Zhang, *Phys. Rev. Lett.*, 2012, **108**, 266806.
35 D.-X. Qu, Y. S. Hor, J. Xiong, R. J. Cava and N. P. Ong, *Science*, 2010, **329**, 821.
36 C. Shekhar, S. Ouardi, A. K. Nayak, G. H. Fecher, W. Schnelle and C. Felser, *Phys. Rev. B: Condens. Matter Mater. Phys.*, 2012, **86**, 155314.
37 C. Shekhar, S. Ouardi, G. H. Fecher, A. K. Nayak, C. Felser and E. Ikenaga, *Appl. Phys. Lett.*, 2012, **100**, 252109.
38 H. G. Johnson, S. P. Bennett, R. Barua, L. H. Lewis and D. Heiman, *Phys. Rev. B: Condens. Matter Mater. Phys.*, 2010, **82**, 085202.
39 L. Thevenod, M. Cassé, W. Desrat, M. Mouis, G. Reimbold, D. K. Maude and F. Boulanger, *Appl. Phys. Lett.*, 2007, **90**, 152111.
40 Y. M. Meziani, J. Lusakowski, W. Knap, N. Dyakonova, F. Teppe, K. Romanjek, M. Ferrier, R. Clerc, G. Ghibaudo, F. Boeuf and T. Skotnicki, *J. Appl. Phys.*, 2004, **96**, 5761.